

Numerical simulations on the propagation of blast wave around a wall

Yuta Sugiyama^{*†}, Tomotaka Homae^{**}, Kunihiro Wakabayashi^{*},
Tomoharu Matsumura^{*}, and Yoshio Nakayama^{*}

^{*}National Institute of Advanced Industrial Science and Technology (AIST),
Central 5, 1-1-1 Higashi, Tsukuba, Ibaraki 305-8565, JAPAN
Phone: +81-29-861-0552

[†]Corresponding author: yuta.sugiyama@aist.go.jp

^{**}Toyama National college of Technology,
1-2 Ebie-neriya, Imizu, Toyama 933-0293, JAPAN

Received: April 1, 2014 Accepted: October 7, 2014

Abstract

This paper numerically models the experimental results of Homae *et al.* in order to reveal the effect of a wall on a blast wave. The x , y , and z axes are defined as the direction between the origin and a midpoint of a wall, a horizontal direction vertical to the x axis, and the height direction, respectively. Two cases of a wall, whose parameters are height H , width W and thickness T , are utilized. Φ_w is determined as the azimuth angle of the corner of a wall. The peak overpressure with directional characteristics, which is caused by the reflection and diffraction of the blast wave at a wall, agrees well with the experimental results. The intensifying effect appears in the direction at right angles to Φ_w . A triple point is generated by the reflection of the diffracted blast wave at the symmetric line ($y = 0$), and propagates on the blast wave. Its path shows a unique profile in the plane of the scaled length y^* in the y direction and similarity distance $D^* = (D - D_{e-t})/D_{e-t}$, where D and D_{e-t} denote distance between the explosion center and triple point in the x direction on the blast wave and distance between the explosion center and the origin of the triple point in the x direction.

Keywords : numerical simulation, blast wave, wall, size effect, directional characteristics

1. Introduction

High energetic materials are used widely in industrial technologies, because even a little explosive releases powerful energy instantly. However, an accidental explosion of high explosives is a hazard to people and has the potential to cause extensive damage to property. Means of minimizing the effects of such an explosion have long been investigated. A wall is often used to protect people and property from the blast wave and fragments caused by the explosion¹⁻⁴. When a wall is located near an explosion center, the blast wave reflects and diffracts at the wall. For practical use of a wall, effects such as diffraction and reflection of the blast wave should be evaluated. Homae *et al.* examined the relationship between the azimuth angle, distance, and blast parameters of peak overpressure and positive impulse⁴. The blast parameters show its directional characteristics.

The wall effects have not been examined quantitatively. Numerical simulation can provide much available data, and numerical results are utilized to understand explosion phenomenon quantitatively. We previously validated a multicomponent flow method for modeling a blast wave problem attenuated by a water wall⁵. In the present paper, we model the previous experiments by Homae *et al.*⁴ using three fluids: detonation products of PETN, steel, and air. The governing equations and algorithm for the method are described in section 2. In section 3, we validate our method by comparing our numerical data with the previous experimental results, and our numerical data reveal the mechanism of directional characteristics of the blast wave by a wall.

2. Numerical setup

We developed a multicomponent method⁵ for three

fluids based on the five-equation model proposed by Allaire *et al.*⁶⁾ In the present study, we use three fluids in order to reproduce the previous experiment⁴⁾. The governing equations used here are three-dimensional compressible Euler equations (1) in generalized coordinates, and a volume fraction transport equation for the two fluids (2).

$$\frac{\partial \hat{\mathbf{Q}}}{\partial t} + \frac{\partial \hat{\mathbf{E}}}{\partial \xi} + \frac{\partial \hat{\mathbf{F}}}{\partial \eta} + \frac{\partial \hat{\mathbf{G}}}{\partial \zeta} = \mathbf{0} \quad (1)$$

$$\frac{\partial}{\partial t} \begin{bmatrix} \alpha_1 \\ \alpha_2 \end{bmatrix} + U \frac{\partial}{\partial \xi} \begin{bmatrix} \alpha_1 \\ \alpha_2 \end{bmatrix} + V \frac{\partial}{\partial \eta} \begin{bmatrix} \alpha_1 \\ \alpha_2 \end{bmatrix} + W \frac{\partial}{\partial \zeta} \begin{bmatrix} \alpha_1 \\ \alpha_2 \end{bmatrix} = \begin{bmatrix} 0 \\ 0 \end{bmatrix} \quad (2)$$

where

$$\hat{\mathbf{Q}} = \frac{1}{J} \begin{bmatrix} \alpha_1 \rho_1 \\ \alpha_2 \rho_2 \\ \alpha_3 \rho_3 \\ \rho u \\ \rho v \\ \rho w \\ \rho E \end{bmatrix}, \quad \hat{\mathbf{E}} = \frac{1}{J} \begin{bmatrix} \alpha_1 \rho_1 U \\ \alpha_2 \rho_2 U \\ \alpha_3 \rho_3 U \\ \rho u U + \xi_x p \\ \rho v U + \xi_y p \\ \rho w U + \xi_z p \\ (\rho E + p) U \end{bmatrix}, \quad \hat{\mathbf{F}} = \frac{1}{J} \begin{bmatrix} \alpha_1 \rho_1 V \\ \alpha_2 \rho_2 V \\ \alpha_3 \rho_3 V \\ \rho u V + \eta_x p \\ \rho v V + \eta_y p \\ \rho w V + \eta_z p \\ (\rho E + p) V \end{bmatrix},$$

$$\hat{\mathbf{G}} = \frac{1}{J} \begin{bmatrix} \alpha_1 \rho_1 W \\ \alpha_2 \rho_2 W \\ \alpha_3 \rho_3 W \\ \rho u W + \zeta_x p \\ \rho v W + \zeta_y p \\ \rho w W + \zeta_z p \\ (\rho E + p) W \end{bmatrix}$$

Here, α_i and ρ_i indicate the volume fraction and density of the i -th fluid ($i=1$ for air, 2 for steel, 3 for detonation products). u , v , w , p , and E are the velocities in the x , y , and z directions, the pressure, and the total energy per unit mass, respectively. U , V , and W denote contravariant velocities in the ξ , η , and ζ directions, and J indicates the Jacobian. The ideal gas, stiffened gas, and Jones-Wilkins-Lee (JWL) equations of state are used to model air, steel, and the detonation products, respectively, as shown in Equations (3)-(5). ϵ_i indicates the internal energy per unit mass of the i -th fluid. Their relation is described in Equation (6). Using variables in Equations (1) and (3)-(6), pressure p of multicomponent flow is calculated. Here, $\gamma_1 = 1.4$, $\gamma_2 = 3.71$, and $\pi = 4.41 \times 10^{10}$ are chosen as the thermodynamic parameters in Equations (3) and (4). The thermodynamic parameters of the steel are determined by the method of Cocchi and Saurel⁷⁾. In the present study, when we model steel as a rigid wall boundary condition, the blast wave strength can be estimated. The method of numerical treatment for steel does not affect the results described in this paper, and there is no need to model the steel as a fluid. However, for further study, we will consider the effect of not only steel but also a soft material such as soil. Therefore, in the present study, we applied multicomponent flow method⁵⁾ and modeled steel as a compressible fluid in order to validate our developed method. In the experiment, the explosive consisted of 95 weight % of PETN and 5 weight % of carbon powder.

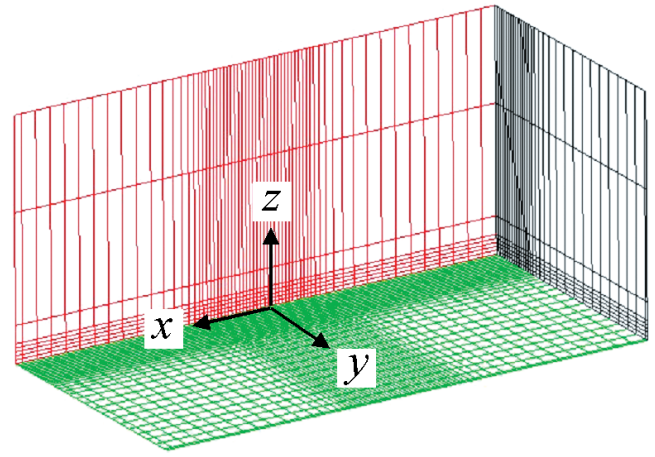


Figure 1 Grid and boundary condition. A symmetric condition (red) at $y=0$ mm, a slip wall condition (green) at $z=0$ mm, and an extrapolation condition at other boundaries (black, only described at $x=-2688$ mm)

Therefore, as a high explosive, the JWL parameters of ρ_0 , A , B , R_1 , R_2 and ω are used for the detonation products of PETN⁸⁾. Initial internal energy per unit mass is an important parameter to determine the strength of the blast wave. We determined it when the peak overpressure without a wall in the case of the present calculation agrees well with that in the case of the previous experiment⁴⁾. Relationship of sound speed of mixture c and each fluid c_i is described in Equation (7).

$$p = (\gamma_1 - 1) \rho_1 \epsilon_1 \quad (3)$$

$$p = (\gamma_2 - 1) \rho_2 \epsilon_2 - \gamma_2 \pi \quad (4)$$

$$p = A \left(1 - \frac{\omega}{R_1} \frac{\rho_3}{\rho_0} \right) \exp \left(-R_1 \frac{\rho_0}{\rho_3} \right) + B \left(1 - \frac{\omega}{R_2} \frac{\rho_3}{\rho_0} \right) \exp \left(-R_2 \frac{\rho_0}{\rho_3} \right) + \omega \rho_3 \epsilon_3 \quad (5)$$

$$\begin{cases} \alpha_1 + \alpha_2 + \alpha_3 = 1 \\ \alpha_1 \rho_1 + \alpha_2 \rho_2 + \alpha_3 \rho_3 = \rho \\ \rho_i E_i = \rho_i \epsilon_i + \frac{1}{2} \rho_i (u^2 + v^2 + w^2) \quad (i = 1, 2, 3) \\ \alpha_1 \rho_1 E_1 + \alpha_2 \rho_2 E_2 + \alpha_3 \rho_3 E_3 = \rho E \end{cases} \quad (6)$$

$$\begin{aligned} \rho \xi c^2 &= \sum_i \rho_i \alpha_i \xi_i c_i^2, \\ \text{where } c_i^2 &= \left(\frac{\partial p}{\partial \rho_i} \right)_{\epsilon_i} + \frac{p}{\rho^2} \left(\frac{\partial p}{\partial \epsilon_i} \right)_{\rho_i}, \quad \xi_i = \left(\frac{\partial \rho_i \epsilon_i}{\partial p} \right)_{\rho_i}, \\ \xi &= \sum_i \alpha_i \left(\frac{\partial \rho_i \epsilon_i}{\partial p} \right)_{\rho_i} \end{aligned} \quad (7)$$

In the present study, we use Harten-Lax-Leer type (HLL) schemes in order to model contact surfaces and maintain accuracy with strong shock waves correctly. We adopt the HLL/HLLC (HLL for Contact) scheme^{5), 9)-12)} for spatial integration, and conduct third-order MUSCL interpolation with a linear scaling limiter¹³⁾. The switching of the HLL and HLLC schemes is determined by the pressure ratio between a grid point and the other points around it. When the pressure ratio is larger than 2, HLL scheme is adapted. The third-stage TVD Runge-Kutta method¹⁴⁾ is used for time integration. Figure 1 shows the grid and boundary

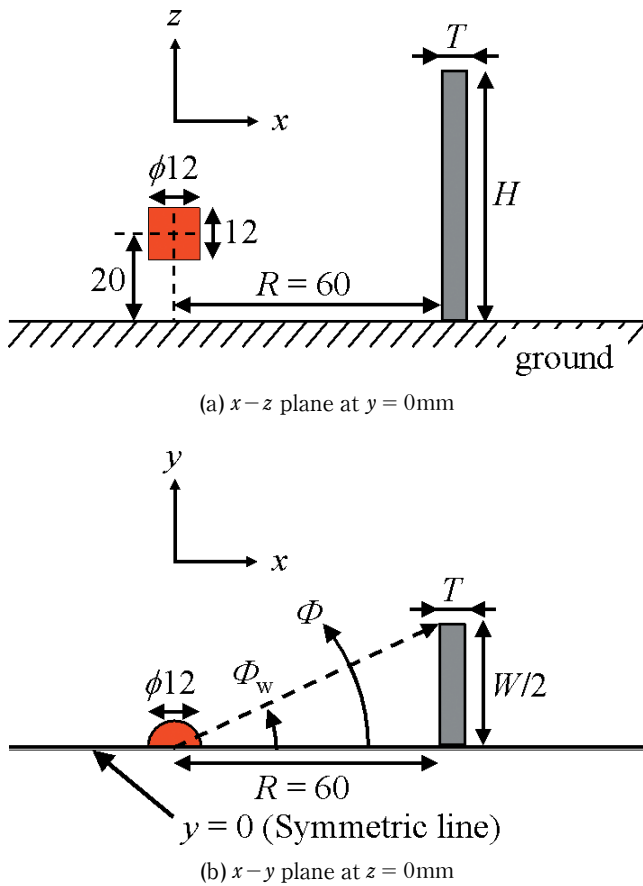


Figure 2 Initial condition with a wall on (a) the $x-z$ plane at $y = 0\text{mm}$ and (b) the $x-y$ plane at $z = 0\text{mm}$. The definitions of azimuth angles Φ and Φ_w are described in (b).

conditions in the present study. The finest and constant grid spacing of 2mm is set at $-600\text{mm} \leq x \leq 600\text{mm}$, $0\text{mm} \leq y \leq 600\text{mm}$, and $0\text{mm} \leq z \leq 200\text{mm}$. In other regions, the grid spacing gradually increases. In order to show the directional characteristics on the ground ($z = 0\text{mm}$), the coarsest grid spacing is limited to 8mm in the x and y directions at $x < -600\text{mm}$, $600\text{mm} < x$, and $600\text{mm} \leq y$. A symmetric condition (red) at $y = 0\text{mm}$, a slip wall condition (green) at $z = 0\text{mm}$, and the extrapolation condition from the first grid near the boundary at other boundaries (black, only described at $x = -2688\text{mm}$) are employed. Figure 2 shows the initial condition with a wall in (a) the $x-z$ plane at $y = 0\text{mm}$ and (b) the $x-y$ plane at $z = 0\text{mm}$. The center of the explosive was located at $x = 0\text{mm}$, $y = 0\text{mm}$, and $z = 20\text{mm}$. Distance, R , from the explosion center to the wall is constant at 60mm. The shape, size, and mass of detonation products are cylindrical with a diameter and length of 12mm and 1.4g. The origin of the azimuth angle Φ is a line passing through the explosion center and the midpoint of the wall in the $x-y$ plane. As shown in Figure 2b, azimuth angle of a wall Φ_w is defined as the angle between $y = 0$ and a line passing through the center of the detonation products and the corner of the wall. The height H , width W and thickness T of a wall are parameters in the present study. Case 1 ($H : 64\text{mm}$, $W : 108\text{mm}$, $T : 6\text{mm}$) models the previous experiments by Homae *et al.*⁴⁾, whereas case 2 ($H : 48\text{mm}$, $W : 48\text{mm}$, $T : 6\text{mm}$) is utilized to discuss the size of a

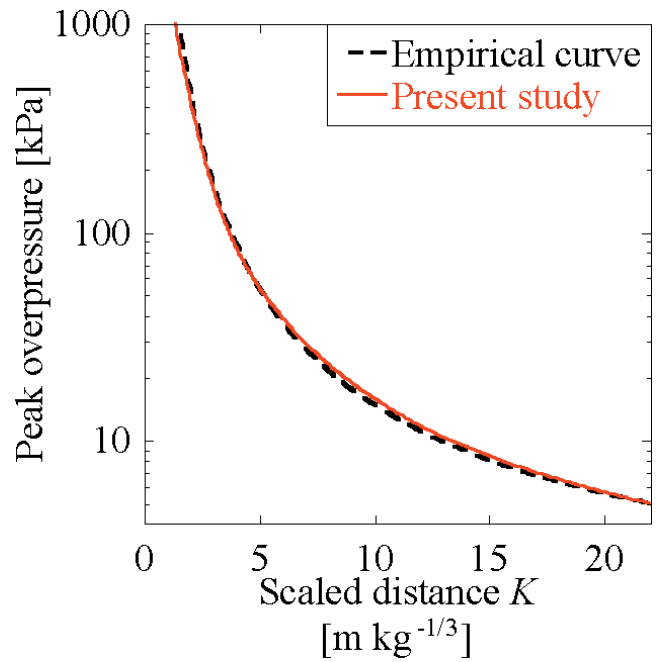


Figure 3 Peak overpressure distributions of the previous experiment⁴⁾ and the present study without a wall.

wall, and the reflection and diffraction of a blast wave. Azimuth angles of walls Φ_w are around 41° for case 1 and 20° for case 2. Grid validation study is conducted in the case without a wall. Figure 3 shows the peak overpressure distributions of the previous experiment⁴⁾ and the present study without a wall. The distribution compares with an empirical curve by the previous experiment⁴⁾. We confirmed that the peak overpressure agrees well with the empirical curve. This indicates that the grid resolution is sufficient to accurately calculate the explosion and blast wave propagation.

3. Results

Our data, as well as those from the experiments of Homae *et al.*⁴⁾, incorporate a scaled distance K , $\text{m kg}^{-1/3}$. A scaled distance of $1 \text{ m kg}^{-1/3}$ corresponds to 118mm in the present study. The experimental data were fitted using a spline function. The peak overpressures are determined from the fitted curve. For safety analysis, we focus on the peak overpressures and propagation of the blast wave on the ground. Figure 4 shows the relationship between azimuth angle Φ and the normalized peak overpressures of (a) $\Phi_w = 41^\circ$ and (b) $\Phi_w = 20^\circ$ at $K = 5.4, 9.5, 13.5, 17.6$, and 21.7. At the larger scaled distance ($K \geq 13.5$), the normalized peak overpressures of the experimental data converge to constant values. Therefore, they are averaged values at $K = 13.5, 17.6$, and 21.7. Peak overpressures are normalized with respect to those in the case without a wall for the present numerical simulations and the previous experiment⁴⁾. Since the reflection and diffraction effects at the wall create a disturbed blast wave, the directional characteristics are observed. The peak overpressures of simulated data in Figure 4a agree well with those of the previous experiment. The tendency for the azimuth angle Φ does not change at large scaled distances ($K \geq 13.5$) in Figure 4. The normalized peak overpressure shows the

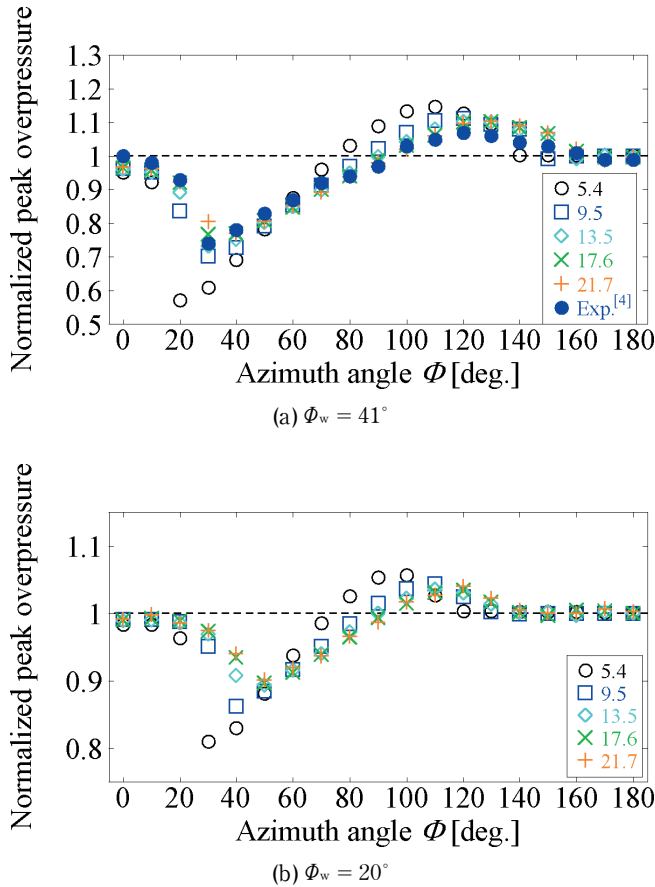


Figure 4 Relationship between azimuth angle Φ and the normalized peak overpressures of (a) $\Phi_w = 41^\circ$ and (b) $\Phi_w = 20^\circ$ at $K = 5.4, 9.5, 13.5, 17.6,$ and 21.7 .

smallest value of 0.75 around $\Phi = 30^\circ$ and the largest value of 1.1 around $\Phi = 130^\circ$ in Figure 4a, and the smallest value of 0.9 around $\Phi = 50^\circ$ and the largest value of 1.03 around 110° in Figure 4b. This indicates that a larger wall provides larger mitigation and intensification effects on the peak overpressures and that the azimuth angles obtaining the largest and smallest peak overpressures depend on Φ_w .

To discuss the directional characteristics on the ground, we utilize the flow patterns in the case of $\Phi_w = 41^\circ$. Figures 5 and 6 show the pressure distributions in the $x-y$ plane (left pictures) at $z = 0$ (on the ground) and as a three-dimensional view (right pictures). Figure 5 shows the snapshots at (a) the reflection ($25.8 \mu\text{s}$) and (b) diffraction of blast wave ($65.3 \mu\text{s}$) on the wall. Figure 6 shows the snapshots of (a) the origin of the triple point ($315.2 \mu\text{s}$), where three shock waves (incident shock, reflected shock, and Mach stem) meet, and (b) the propagation of the triple point ($3165 \mu\text{s}$) on the blast wave. After the diffraction on the wall, the diffracted shock wave collides with $y = 0$ ($\Phi = 0^\circ$) on the ground, and the triple point is generated and propagates on the blast wave in Figure 6b. Since the Mach stem recovers the strength of the diffracted blast wave near $\Phi = 0^\circ$, the peak overpressure shows a convex downward distribution, as shown in Figure 4, and the movement of the triple point is important for understanding the wall effect on the blast wave. The important physics induced by the wall are reflection, diffraction, and the generation and movement of

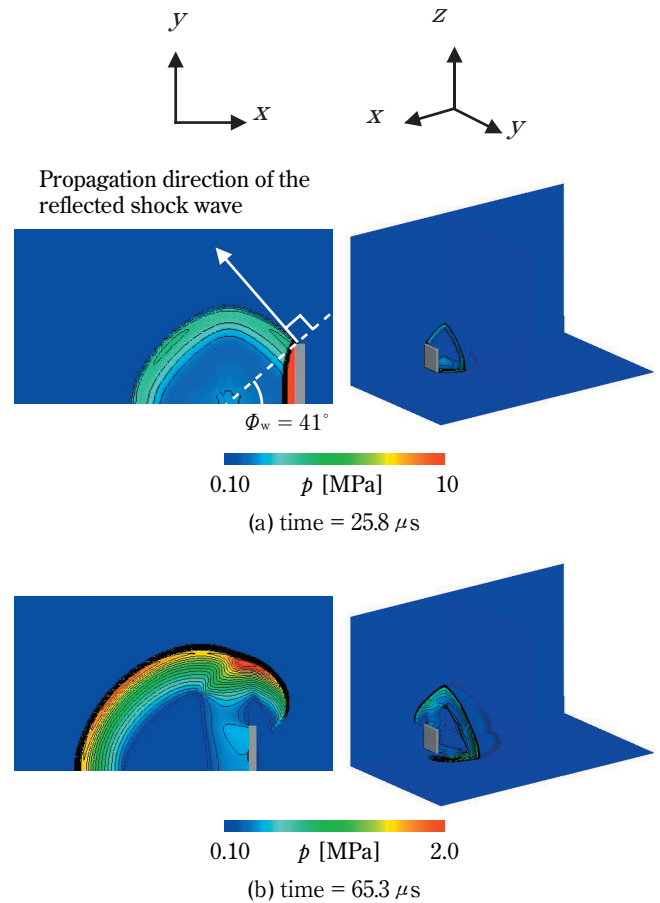


Figure 5 Snapshots at (a) the reflection ($25.8 \mu\text{s}$) and (b) diffraction ($65.3 \mu\text{s}$) of the blast wave on the wall.

the triple point. This paper quantitatively and separately clarifies their effects.

In Figure 5a, the reflected shock wave is generated and propagates on the blast wave. After the shock wave reflects on the wall, the reflected shock wave propagates normal to the incident angle between wall and the shock wave, the intensifying effect of the blast wave on the reflection appears in the direction at right angles to Φ_w described as a white arrow in Figure 5a. Therefore, the largest peak overpressures appear at $\Phi = 130^\circ$ in the case of $\Phi_w = 41^\circ$ and at $\Phi = 110^\circ$ in the case of $\Phi_w = 20^\circ$.

To discuss the shape of the diffracted blast wave and the origin of the triple point, we use the Whitham theory¹⁵⁾, which is an approximate treatment using the method of characteristics and gives information on the shape of a two-dimensional diffracted shock wave. Since kinematic relations are written in characteristic form, it is adapted only when Mach number is larger than 1.0. The predictions of shock front shape by the Whitham theory have been very successful and have been applied to a variety of situations, including the diffraction of a shock wave over a curved arc¹⁶⁾. We assume as follows: the blast wave near a wall propagates perpendicular to the wall since the wall works as a current plate for the blast wave, and, the diffraction effect in the z direction is negligible since two-dimensional diffraction in x and y directions determines the blast wave shape on the ground.

Figure 7a shows the shape of the diffracted shock wave as described by the Whitham theory. The initial planar

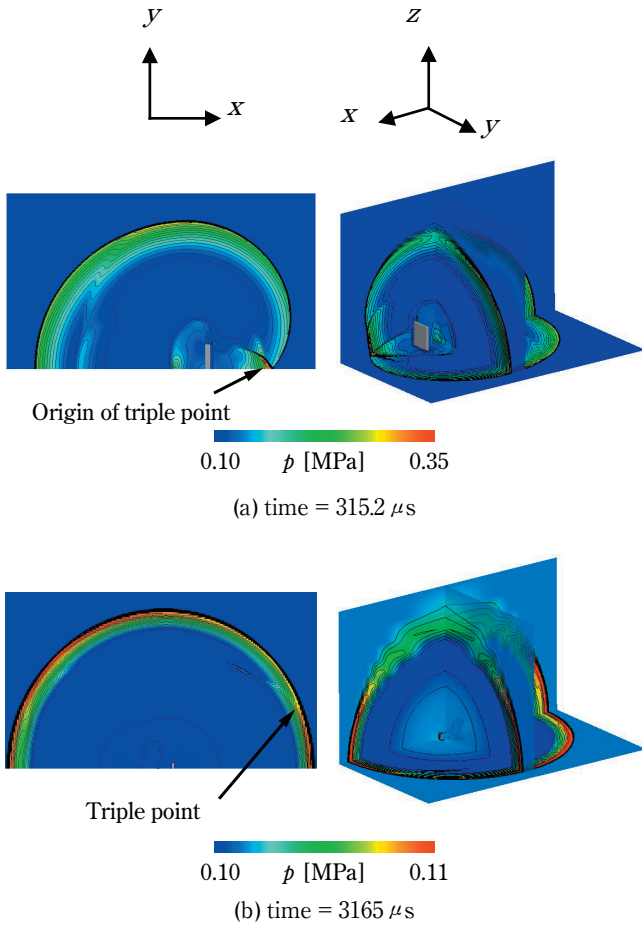
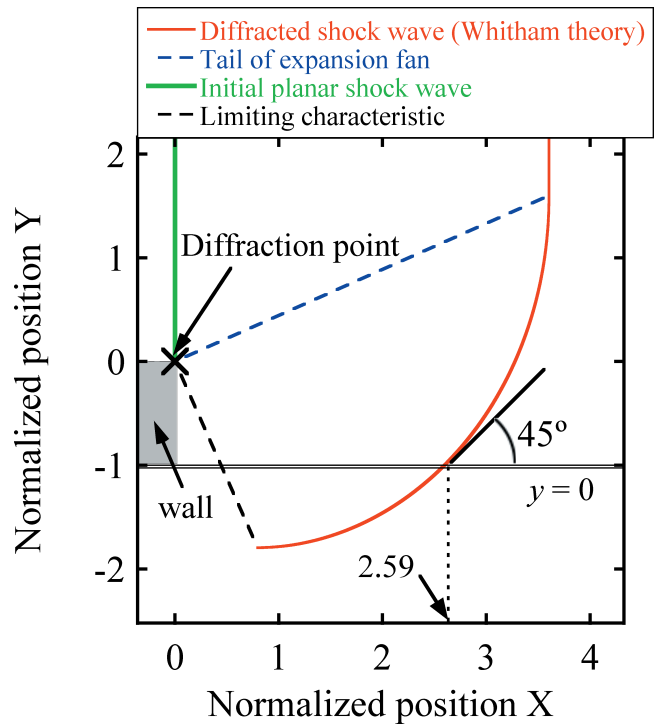


Figure 6 Snapshots of (a) the generation of the triple point ($315.2 \mu\text{s}$), where three shock (incident shock, reflected shock and Mach stem) meet, and (b) the propagation of the triple point ($3165 \mu\text{s}$) on the blast wave.

shock wave indicates the initial condition of the Whitham theory. The origin in Figure 7a denotes the start point of the diffraction. As the shock wave diffracts, expansion wave appears from the wall. The expansion affect the shock wave from the tail of the expansion fan to the limiting characteristic. Red line denotes the similarity shape of the fully developed and diffracted shock wave. Additionally, we illustrate a virtual wall and $y=0$ (symmetric line). The horizontal and vertical axes (X, Y) are normalized with respect to the half-width of the wall, $W/2$. A previous study¹⁷⁾ showed that a triple point appears upon occurrence of an explosion with a moderate height of burst above ground. For moderate heights of burst, a triple point occurs at a distance from ground zero approximately equal to the burst height, and the incident angle between blast wave and the ground is 45° . Therefore, we focus on the angle between the diffracted blast wave and $y=0$, which becomes 45° , and X is estimated as 2.59. Figures 7b and 7c show the instantaneous pictures in the cases of $\Phi_w = 41^\circ$ and $\Phi_w = 20^\circ$, respectively, and superimpose on the diffracted shock wave predicted by the Whitham theory when the triple point is generated. The shock shape near $y=0$ agrees well with that predicted by the Whitham theory. Since the blast wave expands spherically, the diffracted shock shape far from $y=0$ does not agree with that



(a) Shape of the diffracted shock wave predicted by Whitham theory

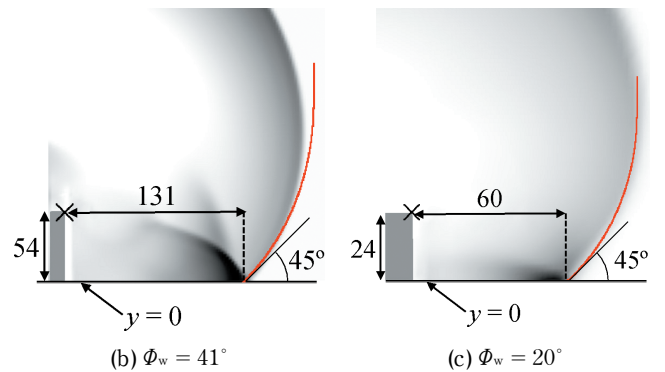


Figure 7 (a) Shape of the diffracted shock wave predicted by Whitham theory. (b) and (c) the instantaneous pictures of the diffracted shock wave when the triple point is generated in the cases of $\Phi_w = 41^\circ$ and $\Phi_w = 20^\circ$ in the $x-y$ plane, respectively. The origin in (a) denotes the start point of the defraction. The horizontal and vertical axes (X, Y) are normalized with respect to the half-length of the wall, $W/2$. Red curves in (b) and (c) denote the shape of the diffracted shock wave by Whitham theory.

predicted by the Whitham theory. Distances and normalized position X between the wall and the position of the origin of the triple point are 131 mm and 2.43 in Figure 7b, and 60 mm and 2.50 in Figure 7c. The normalized positions X agree with the theoretical value of 2.59 in Figure 7a. Therefore, the Whitham theory allows an estimate of the shape of the diffracted blast wave by a wall near $y=0$. At the position where the angle between the blast wave and $y=0$ becomes 45° , the triple point is generated.

Estimating the position of the triple point on the blast wave such as that shown in Figure 6b is important, since the triple point recovers the strength of the diffracted blast wave. Huber and McFarland¹⁸⁾ show that the

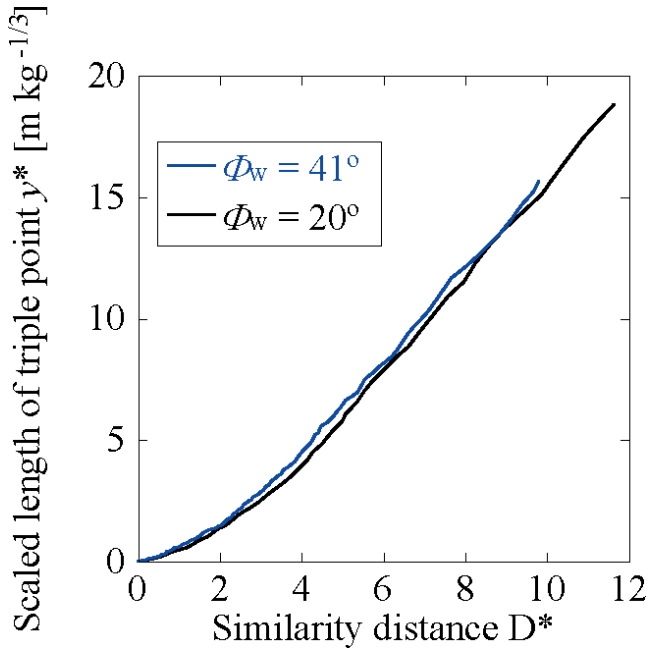


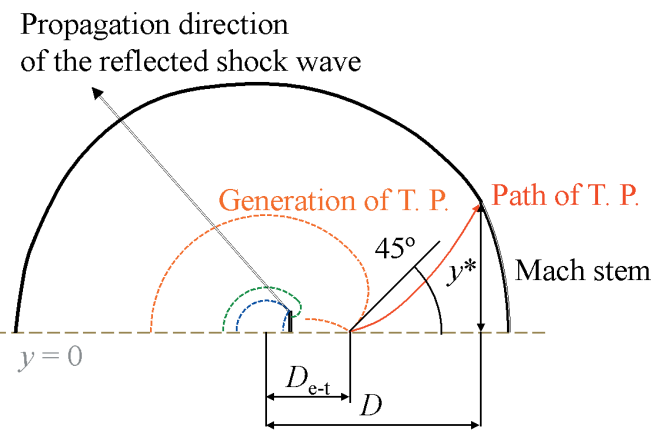
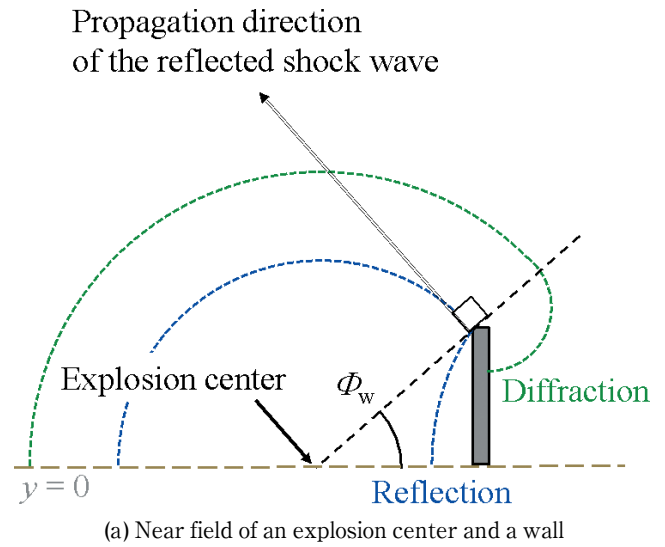
Figure 8 Path of the triple point in D^*-y^* plane. The horizontal axis indicates the similarity distance $D^* = (D - D_{e-t})/D_{e-t}$, y^* indicates the scaled length of triple point in the y direction.

greatest similarity of the triple point data for various heights of burst was found when the scaled height of the triple point (in the z direction), h^* , from the ground was plotted with similarity distance $D^* = (D - D_{e-t})/D_{e-t}$, where D denotes distance in the x direction between the explosion center and the triple point on the blast wave. In the present study, $D_{e-t} = 197\text{mm}$ for $\Phi_w = 41^\circ$ and $D_{e-t} = 131\text{mm}$ for $\Phi_w = 20^\circ$ on the ground. Then, we apply their idea and plot the path of triple point in the D^*-y^* plane in Figure 8, where y^* indicates the scaled length of the triple point in the y direction. The path of the triple point shows a unique profile in the present study, as well as in those by Huber and McFarland, and the similarity distance D^* is useful for understanding the path of the triple point. From Figure 7, the theoretical distance between a wall and the origin of the triple point is $2.59W/2$, and therefore, D_{e-t} is estimated as $R + T + 2.59W/2$, where R and T denote distance from the explosion center to the wall and the thickness of the wall, respectively.

4. Conclusion

We numerically modeled previous experimental results and quantitatively revealed the effect of a wall on a blast wave. Our study gave a schematic picture in the $x-y$ plane on the ground as shown in Figure 9 with the wall effects, such as reflection and diffraction and the propagation of triple point.

1. Since the reflected shock wave propagates perpendicular to the blast wave, the intensifying effect of the blast wave on the reflection appears in the direction at right angles to Φ_w .
2. The Whitham theory allows an estimate of the shape of the diffracted blast wave by a wall near $y = 0$. At the position where the angle between the blast wave and $y = 0$ becomes 45° , the triple point is generated.



- D_{e-t} : distance between explosion center and the origin of triple point
- D : distance between explosion center and triple point on the blast wave

Figure 9 Schematic diagram showing wall effects: the reflection and diffraction, and the propagation of the triple point in the $x-y$ plane. T. P. denotes the triple point.

Distance in the x direction between the explosion center and the origin of the triple point D_{e-t} is estimated as $R + T + 2.59W/2$, where R , T , and W denote the distance from the explosion center to the wall, the thickness of the wall, and the width of the wall, respectively.

3. The path of the triple point shows a unique profile in the plane of the scaled length y^* in the y direction and similarity distance $D^* = (D - D_{e-t})/D_{e-t}$, where D and D_{e-t} denote distances in the x direction between the explosion center and the triple point on the blast wave and between the explosion center and the origin of the triple point, respectively.

Reference

1) S. Sudo, J. Industrial Explosives Society (Sci. Tech. Energetic Materials), 23, 160 (1962) (in Japanese).

- 2) Y. Mizushima, J. Industrial Explosives Society (Sci. Tech. Energetic Materials), 31, 361–377 (1970).
- 3) T. Homae, T. Matsumura, K. Wakabayashi, and Y. Nakayama, Sci. Tech. Energetic Materials, 69, 92–97 (2008).
- 4) T. Homae, T. Matsumura, K. Wakabayashi, and Y. Nakayama, Sci. Tech. Energetic Materials, 72, 155–160 (2011).
- 5) Y. Sugiyama, Y. Homae, K. Wakabayashi, T. Matsumura, and Y. Nakayama, Science and Technology of Energetic Materials, 75, 112–118 (2014).
- 6) G. Allaire, S. Clerc, and S. Kokh, J. Comput. Phys. 181, 577–616 (2002).
- 7) J.-P. Cocchi and R. Saurel, Journal of Computational Physics, 137, 265–298 (1997).
- 8) E. Lee, M. Finger, and W. Collins, LLNL report, UCID-16189, (1973)
- 9) A. Harten, P.D. Lax, and B. van Leer, SIAM Review 25, 35–61 (1983).
- 10) B. Einfeldt, SIAM J. Numer. Anal. 25, 294–318 (1988).
- 11) E. F. Toro, M. Spruce, and W. Speares, Shock Waves 4, 25–34 (1994).
- 12) S. D. Kim, B.J. Lee, H.J. Lee, I.-S. Jeung, and J.-Y. Choi, Int. J. Numer. Meth. Fluids 62, 1107–1133 (2010).
- 13) X. Zhang and C.-W. Shu, Proc. R. Soc. A 467, 2752–2776 (2011).
- 14) C.-W. Shu and S. Osher, J. Comput. Phys. 77, 439–471 (1988).
- 15) G. B. Whitham, J. Fluid Mech. 2, 145–171 (1957).
- 16) B. W. Skews, Shock Waves 14 (3), 137–146 (2005).
- 17) S. Glasstone and P.J. Dolan, The effects of Nuclear Weapons, 3rd ed. (Washington, DC : Dept. of Defence) (1977).
- 18) P. W. Huber and D.R. McFarland, NASA Technical Report R-23, 1–25, (1959).